Editors' Suggestion | Featured in Physics

Helical Locomotion in Yield Stress Fluids

Farshad Nazari,[1] Kourosh Shoele,[2] and Hadi Mohammadigoushki[1,*]
[1]Department of Chemical and Biomedical Engineering, FAMU-FSU College of Engineering, Tallahassee, Florida 32310, USA
[2]Department of Mechanical Engineering, FAMU-FSU College of Engineering, Tallahassee, Florida 32310, USA

(Received 27 March 2022; accepted 27 January 2023; published 16 March 2023)

We report three stages for locomotion of a helical swimmer in yield stress fluids. In the first stage, the swimmer must overcome the material's yield strain to generate rotational motion. However, exceeding the first threshold is not sufficient for locomotion. Only when the viscous forces are sufficiently strong to plastically deform the material to a finite distance away from the swimmer will net locomotion occur. Once locomotion is underway in the third stage, the yield stress retards swimming at small pitch angles. Conversely, at large pitch angles, yield stress dominates the flow by enhancing swimming speed. Flow visualizations reveal a highly localized flow near the swimmer in yield stress fluids.

DOI: 10.1103/PhysRevLett.130.114002

Microorganism locomotion is important in our daily life, environment, and physiology [1]. For example, penetration of *Helicobacter pylori* through gastric mucus may cause ulcers and cancer [2–4], burrowing nematode worms through wet soil can enhance soil aeration and fertility [5,6], motility of bacteria may infect food products, and hydrogels are used as tissue scaffolds and biofilms [7,8] or give rise to a new set of advanced biosensors and biofilters [9,10]. Rheological measurements indicate that these fluidic environments display a strong yield stress behavior [3,6,11]. Therefore, motility of organisms in yield stress fluids is important in a host of applications, and its mechanistic understanding provides fundamental insights that can inform scientists on how to mitigate those health risks or design and engineer new materials for advanced applications. Despite admirable progress in our understanding of locomotion in polymeric fluids [12–21], little is known about locomotion in yield stress fluids.

Yield stress materials behave like a solid and barely deform below the yield stress threshold. A recent experimental study showed that, while at high pH (near neutral) *H. pylori* swims in porcine gastric mucus (PGM) freely [4,22], at low pH (at which PGM is a yield stress fluid [3,23]) *H. pylori* is stuck in PGM [4,22]. A relevant theoretical study of Balmforth and co-workers showed that, below a critical Bingham number, the yield stress impedes the locomotion of a 2D undulatory swimmer near a solid boundary in a simple Bingham fluid model [24]. The Bingham number is defined as $Bi = \sigma_y/\eta\dot{\gamma}$, where σ_y, η, and $\dot{\gamma}$ denote the yield stress, viscosity, and the rate of deformation, respectively. Although these studies hint at the existence of some critical thresholds that must be overcome by organisms to gain motility in yield stress materials, such critical thresholds have not been quantified in experiments. Furthermore, only a limited theoretical effort has been devoted to probing swimming mechanisms, post yielding, in yield stress fluids [25–28]. Particularly, Hewitt and Balmforth developed a slender body theory for yield stress fluids and found that the optimal pitch angle associated with maximum swimming speed is moderately larger than the calculated one for Newtonian fluids [26,27]. More recently, Eastham, Mohammadigoushki, and Shoele investigated locomotion of a squirmer in a Bingham fluid model [28]. Despite these advances, there is a dearth of experimental studies that address the mechanisms of locomotion in yield stress fluids. Here, we present the first experimental investigation of locomotion in yield stress fluids. We identify and document, for the very first time, two critical thresholds that must be overcome by the swimmer in order to propel itself forward in yield stress fluids. Furthermore, we show that the yield stress enriches the fluid dynamics once swimming is underway with a complex and localized yielded zone near the swimmer surface accompanied by an unyielded region at a finite distance away from the swimmer.

Inspired by microswimmers such as *H. pylori*, we perform experiments with a 3D printed helical (corkscrew) swimmer. All swimmer's dimensions are held fixed except for the tail pitch angle, which varies as $\psi = 12°$–$74°$. The swimmer is actuated via a uniform magnetic field of a rotating Helmholtz coil (this setup is similar to the one used in our previous study [29] and shown in Fig. S1 in Supplemental Material [30]). A combination of particle tracking velocimetry and particle image velocimetry (PIV) is utilized to measure the swimming speed and to visualize the flow field around the swimmer. Yield stress fluids based on Carbopol solutions are considered. Additionally, Newtonian fluids based on corn syrup are prepared for the purpose of comparison with the results obtained in yield stress fluids. The rheological properties of these fluids are reported in Table S1 and Fig. S2 [30].

The locomotion of the helical swimmer in yield stress fluids can be divided into three stages. The first stage is associated with a minimum torque needed to generate rotational motion. Below a critical torque ($\mathcal{T}_Y$), the swimmer does not have enough power to overcome the elastic resistance of the yield stress medium and, therefore, cannot rotate with the rotating magnetic field of the Helmholtz coil (see Movie S1 and Fig. S3 [30]). Our hypothesis is that, in stage I, the yield stress around the swimmer transitions from a fully recoverable elastic network to a permanently plastic fluid and that triggers rotational motion. To test this hypothesis, we define a yield strain as

$$\varepsilon_Y = \frac{\tau_Y}{G_o}, \tag{1}$$

where τ_Y and G_o are the stress needed for the material to yield around the swimmer and the elastic modulus of the material, respectively. Here, $\tau_Y \cong (\mathcal{T}_Y/A.L)$, where A and L are the total surface area and length of the swimmer, respectively (see caption of Fig. S3 [30]). Figure 1 shows that, while the minimum yield strain needed to initiate rotational motion is independent of the swimmer's pitch angle, it increases by the yield stress of the material. To further analyze these data, we measured the yield strain of these fluids via a commercial rheometer (ε_c; see Fig. S4 [30]). The inset in Fig. 1 shows that the ratio of these two yield strain values is remarkably close to unity. The latter result not only supports our hypothesis on the underlying cause of the first transition in swimming experiments, but also suggests that this swimmer may be used as an *in situ* rheometer with potentially some broader impacts. For example, a magnetically actuated helical microswimmer robot could be used as an *in situ* rheometer to characterize the yield strain of valuable biological gels and tissues that are not accessible in large quantity for bulk rheological measurements. Exceeding the first threshold is yet not sufficient for locomotion. In fact, for $\varepsilon > \varepsilon_Y$ and below a critical rotational velocity ($\Omega < \Omega_c$), the swimmer enters a second stage at which, despite in-place rotational motion, net locomotion cannot be achieved [see Fig. 2(a)]. We checked that this critical rotational velocity is a strong function of yield stress and the swimmer's pitch angle (shown in Fig. S6 [30]). Our hypothesis is that this critical threshold is controlled by a balance between viscous and yield stresses, which is captured through the Bingham number defined here based on the shear-thinning viscosity $\eta(\dot{\gamma})$, and a characteristic shear rate of $\dot{\gamma} = R\Omega/R = \Omega$, with R being the radius of the swimmer's cross section. Figure 2(b) shows that through a Bingham number we can collapse all critical rotational velocities into a single graph over a broad range of swimmer pitch angles and fluid rheological properties. Note that, above this critical Bingham $Bi_c \approx 0.6$, a rotating swimmer does not generate net locomotion. Finally, swimmers with larger pitch angles ($\psi \geq 37°$) always undergo locomotion even at the lowest accessible imposed rotation rates ($\Omega_{\min} = 4 \times 10^{-3}$ Hz).

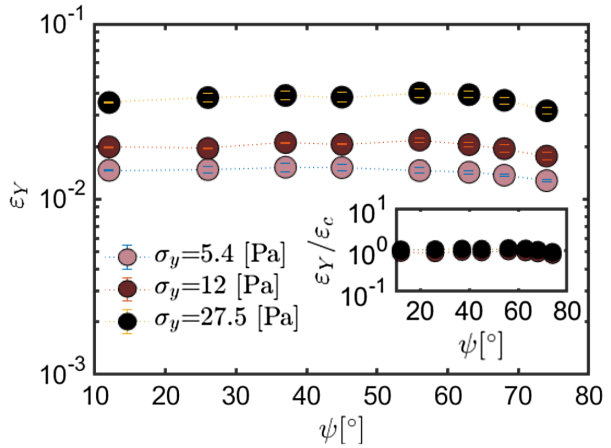

FIG. 1. The critical yield strain as a function of the swimmer's pitch angle in various yield stress fluids. The inset shows the ratio of yield strain obtained from swimming experiments to those measured in a commercial rheometer.

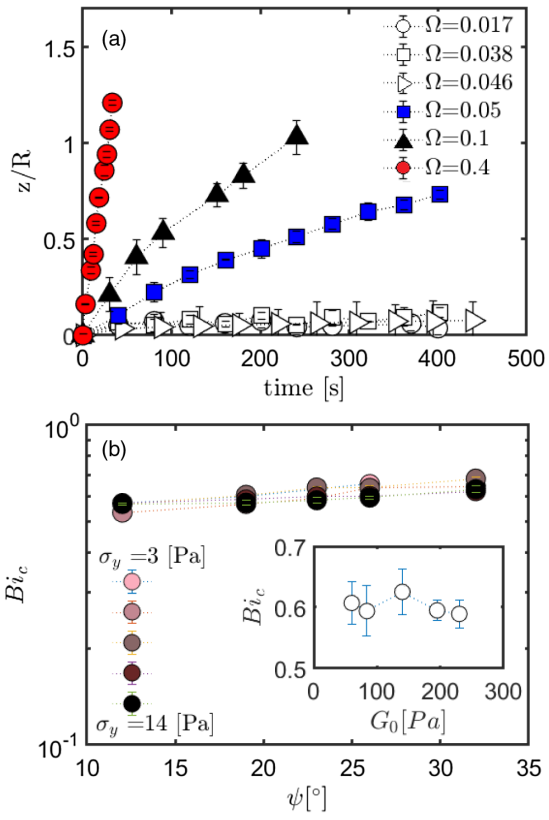

FIG. 2. (a) The trajectory of a swimmer with a pitch angle $\psi = 26°$ as a function of time for different imposed rotation rates in a fluid with $\sigma_y = 5.4$ [Pa]. (b) The critical Bingham number associated with the onset of swimming as a function of pitch angle $\psi[°]$ for various yield stress fluids. The inset shows the critical Bingham number as function of plateau modulus G_0.

By overcoming the above two critical thresholds (ε_Y and Bi_c), the swimmer enters stage III of locomotion, at which it is propelled at a constant velocity U. Figure 3(a) shows the normalized swimming speed ($U/R\Omega$) as a function of the pitch angle for the Newtonian and sample yield stress fluids for $Bi < Bi_c$. Below the critical Bingham number, we observe that $U/R\Omega$ in the yield stress fluids is constant at different imposed rotation rates (see Fig. S6 [30]). Therefore, Fig. 3(a) shows the averaged swimming speed over a broad range of imposed rotation rates above Ω_c. Additionally, we confirmed that $U/R\Omega$ is independent of the viscosity of the Newtonian fluid consistent with the resistive force theory [31,32]. Figure 3(a) provides three important and novel aspects of swimming in yield stress fluids. First, at low pitch angles ($12° \leq \psi \leq 37°$), the swimming speed in the yield stress fluids is lower than those measured in the Newtonian fluid. As the yield stress increases in this range of pitch angles, the swimming speed further decreases and approaches zero [see Fig. 3(b)]. These yield stress fluids are strongly shear thinning, and shear thinning has been known to enhance swimming speed of helical swimmers [33,34]. Hence, for these pitch angles, the yield stress dominates the flow by resisting against locomotion, and shear-thinning effects are negligible.

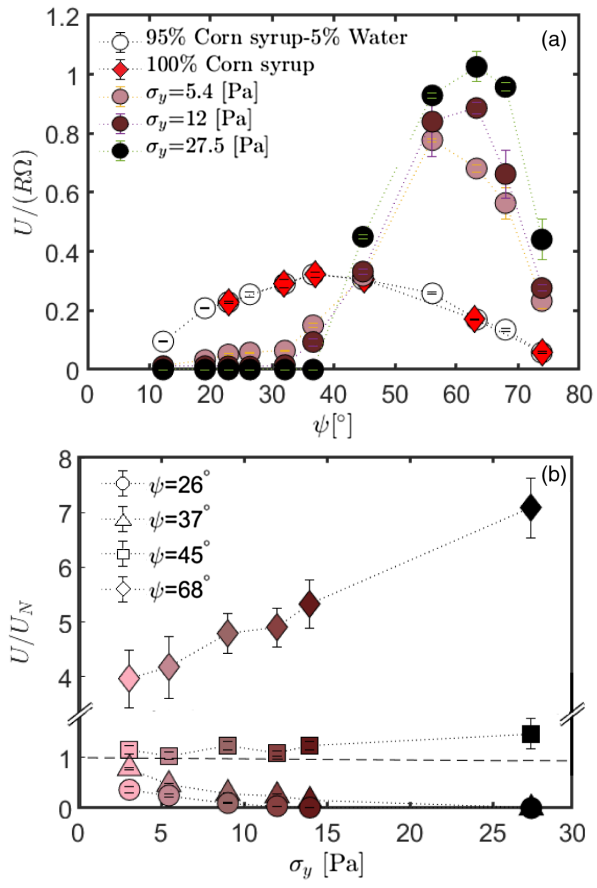

FIG. 3. (a) Normalized swimming speed $U/(R\Omega)$ as a function of pitch angle ψ[°] for various swimmers in yield stress fluids and Newtonian fluids. (b) Swimming speed normalized by the Newtonian speed (U/U_N) as a function of σ_y for swimmers with different pitch angles. In (b), the comparison is performed at the same imposed rotational velocity.

For $\psi = 45°$, the swimming speed in the yield stress fluid is similar to those measured in the Newtonian fluid, and by increasing the yield stress this ratio changes modestly [see Fig. 3(b)]. For larger pitch angles $\psi > 45°$, the swimming speed in the yield stress fluid is much larger than those measured in the Newtonian fluids, and increasing the yield stress further enhances the swimming speed [see Fig. 3(b)]. In shear-thinning fluids with a shear-thinning index of $n = 0.47$–0.9, the maximum swimming enhancement has been noted to be about 50% [34]. We surmise from these results that, although shear thinning might have contributed to swimming enhancement at large pitch angles, the swimming dynamics are primarily controlled by the yield stress. Finally, the optimal pitch angle in the yield stress fluid has shifted to much larger values compared to the Newtonian fluid (e.g., $\psi \approx 56°$ and $\psi \approx 63°$ for fluids with $\sigma_y = 5.4$ and $\sigma_y = 27.5$, respectively). The latter result is consistent with predictions of the slender body theory in the Bingham model [26]. Note that the Reynolds number is very small in these experiments, and, therefore, inertia does not play any role in these experiments (see Table S1 [30]).

To better understand the physics underlying the above stages of locomotion in yield stress fluids, we analyzed the detailed form of flow field around the swimmer. In stage I, no net motion is observed. Hence, the fluid is stationary around the swimmer and PIV does not detect any motion. Figures 4(a)–4(h) show a series of time-averaged two-dimensional velocity profiles around the swimmer in stages II and III of locomotion (see Movie S2 and S3 [30]). Recall that in stage II, despite in-place rotation, a swimmer cannot generate net locomotion. In particular, Fig. 4(a) shows that in stage II of locomotion and at high Bingham numbers ($Bi > Bi_c$; e.g., $Bi = 0.68$), while a weak propulsion is observed in the interior region of the helix in the $r-z$ plane, the fluid around the swimmer's head in the $r-\theta$ plane does not deform due to the presence of a significant wall slip [albeit within the precision of our PIV measurements; see Figs. 4(e) and 4(i)]. This result is similar to experimental findings of Daneshi *et al.* [35] that showed capillary flows of yield stress fluids at low pressure gradients produce a fully plug flow with a significant wall slip at the walls. As the Bingham number decreases toward Bi_c (e.g., $Bi = 0.63$) and the swimmer approaches stage III of its locomotion, the tail propulsion is boosted [shown in Fig. 4(b)], and the yielded zone in the $r-\theta$ plane is shifted to a finite distance away from the swimmer's surface with a weaker wall slip [see Figs. 4(f) and 4(i)]. The corresponding flow fields in the Newtonian fluid are distinct from those measured in the yield stress fluids (see Fig. S7 [30]). While the velocity of the yield stress fluid decays quickly and approaches a nonyielded zone at a finite distance (r_σ)

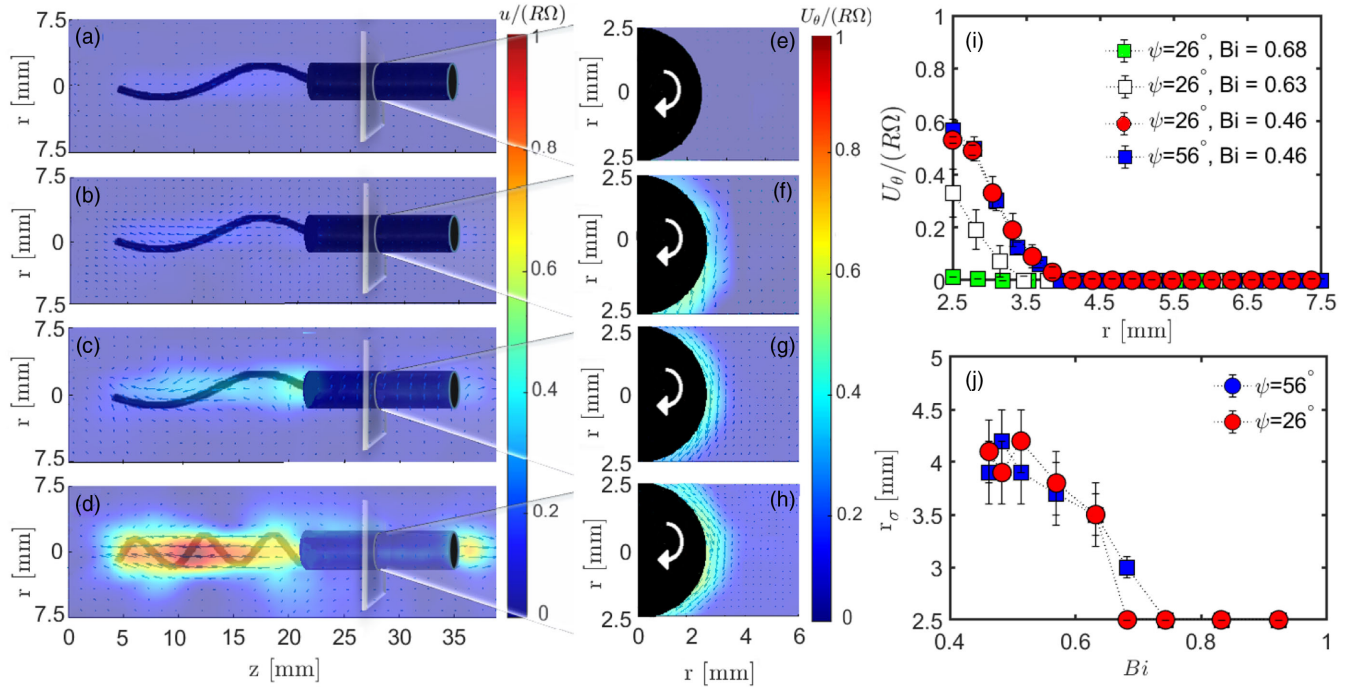

FIG. 4. Time-averaged 2D velocity profiles in the $r-z$ plane [(a)–(d)] and orthogonal to the direction of locomotion [(e),(h)] in a yield stress fluid with $\sigma_y = 5.4$ [Pa]. In (e)–(h), the swimmer is rotating clockwise. Panels (a), (e), (b), (f), (c), (g), and (d), (h) correspond to ($\psi = 26°$, $Bi = 0.68$), ($\psi = 26°$, $Bi = 0.63$), ($\psi = 26°$, $Bi = 0.46$), and ($\psi = 56°$, $Bi = 0.46$), respectively. (i) The time-averaged 1D angular velocity profile as a function of the radial location around the head of the swimmer. (j) Location of the yield surface as a function of the Bingham number for swimmers with different pitch angles. u and U_θ denote the fluid velocity in the z and θ directions, respectively. Finally, the details of the time averaging are given in Fig. S7 [30].

away from the swimmer [Fig. 4(j)], the flow of a Newtonian fluid extends to much farther distances away from the swimmer, despite rotating at the same angular velocities. What these flow visualization findings reveal to us is that, for $Bi > Bi_c$, the swimmer experiences an extremely confined space (and, consequently, a significant drag) around its head in yield stress fluids such that the weak fluid propulsion generated in the interior region of the helix is not strong enough to overcome this drag. Consequently, despite in-place rotation, the swimmer does not progress forward in yield stress fluids.

Next, we investigate the impact of the tail pitch angle on the flow field around the swimmer and discuss the link between such flow fields and swimming speed results in Fig. 3(a). For this purpose, we consider two swimmers with $\psi = 26°$ and $\psi = 56°$ at $Bi = 0.46$ in stage III of their locomotion [cf. Figs. 4(c) and 4(d)]. Figures 4(c) and 4(d) show that, while the propulsion generated in the interior region of the helix is much stronger for the swimmer with a larger pitch angle, the velocity field in the $r-\theta$ plane [Figs. 4(g)–4(i)] and the location of the yield surface [Fig. 4(j)] are the same for the two swimmers. These observations suggest that, although swimmers experience a similar confinement (or drag) around their head, the swimmer with $\psi = 56°$ experiences a stronger thrust and, therefore, should be propelled faster than the swimmer with $\psi = 26°$. This conclusion is consistent with the swimming speed data reported in Fig. 3(a). Again, the corresponding experiments in Newtonian fluid reveal a stark difference with those obtained in yield stress fluid. The Newtonian fluid deforms to much farther distances away from the swimmer surface with a negligible wall slip (see Fig. S8 [30]). These results highlight the strong coupling between a highly localized flow around the swimmer and the swimming dynamics in yield stress fluids.

In summary, we provided the first experimental investigation of the helical locomotion in yield stress fluids and illustrated that swimming can be divided into three stages. In the first stage, the swimmer must create rotational motion by overcoming the yield strain of the material (ε_Y). However, exceeding the first threshold is not sufficient for locomotion. For $Bi > Bi_c$, the yield stress fluid is hardly deformed around the swimmer, and the tail propulsion is not strong enough to generate locomotion. Only below a critical $Bi_c \approx 0.6$, when the rotational motion forces the material to yield at a finite distance away from the swimmer, will forward motion occur. Once swimming is underway in the third stage of locomotion, the swimming speed in the yield stress fluids is lower than those measured in Newtonian fluids for $\psi \leq 37°$. Conversely, for $\psi \geq 45°$, the swimmer moves faster in the yield stress fluids compared to their Newtonian counterparts. These

observations open a new field of study, and, to fully understand them, there are still several questions that need to be answered, including the following. Why has the optimal pitch angle shifted to larger values in the yield stress fluid? What controls optimal swimming in yield stress fluids? What is the role of the swimmer's head? How does changing swimming strategy to a force- or torque-free mode affect the locomotion in yield stress fluids? We hope to address these questions in the near future.

We are grateful to Neil Balmforth and Philipe Coussot for several helpful discussions.

*Corresponding author.
hadi.moham@eng.famu.fsu.edu

[1] E. Lauga and T. R. Powers, The hydrodynamics of swimming microorganisms, Rep. Prog. Phys. **72**, 096601 (2009).
[2] Sebastian Suerbaum and Pierre Michetti, Helicobacter pylori infection, N. Engl. J. Med. **347**, 1175 (2002).
[3] J. P. Celli, B. S. Turner, N. H. Afdhal, R. H. Ewoldt, G. H. McKinley, R. Bansil, and S. Erramilli, Rheology of gastric mucin exhibits a ph-dependent sol-gel transition, Biomacromolecules **8**, 1580 (2007).
[4] R. Bansil, J. P. Celli, J. M. Hardcastle, and B. S. Turner, The influence of mucus microstructure and rheology in helicobacter pylori infection, Front. Immunol. **4**, 310 (2013).
[5] H. Ferris, R. C. Venette, and S. S. Lau, Dynamics of nematode communities in tomatoes grown in conventional and organic farming systems, and their impact on soil fertility, Appl. Soil Ecol. **3**, 161 (1996).
[6] T. A. Ghezzehei and D. Or, Rheological properties of wet soils and clays under steady and oscillatory stresses, Soil Sci. Soc. Am. J. **65**, 624 (2001).
[7] Marion Fischer, Maryam Vahdatzadeh, Rupert Konradi, Jens Friedrichs, Manfred F. Maitz, Uwe Freudenberg, and Carsten Werner, Multilayer hydrogel coatings to combine hemocompatibility and antimicrobial activity, Biomaterials **56**, 198 (2015).
[8] N. Kandemir, W. Vollmer, N. S. Jakubovics, and J. Chen, Mechanical interactions between bacteria and hydrogels, Sci. Rep. **8**, 10893 (2018).
[9] Shardul Bhusari, Shrikrishnan Sankaran, and Aránzazu del Campo, Regulating bacterial behavior within hydrogels of tunable viscoelasticity, Adv. Sci. **9**, 2106026 (2022).
[10] C. Gilbert, T. C. Tang, W. Ott, B. A. Dorr, W. M. Shaw, G. L. Sun, T. K. Lu, and T. Ellis, Living materials with programmable functionalities grown from engineered microbial co-cultures, Nat. Mater. **20**, 691 (2021).
[11] Vivian H. M. Mouser, Ferry P. W. Melchels, Jetze Visser, Wouter J. A. Dhert, Debby Gawlitta, and Jos Malda, Yield stress determines bioprintability of hydrogels based on gelatin-methacryloyl and gellan gum for cartilage bioprinting, Biofabrication **8**, 035003 (2016).
[12] Gaojin Li, Eric Lauga, and Arezoo M. Ardekani, Microswimming in viscoelastic fluids, J. Non-Newtonian Fluid Mech. **297**, 104655 (2021).
[13] Alison E. Patteson, Arvind Gopinath, and Paulo E. Arratia, Active colloids in complex fluids, Curr. Opin. Colloid Interface Sci. **21**, 86 (2016).
[14] S. E. Spagnolie, B. Liu, and T. R. Powers, Locomotion of Helical Bodies in Viscoelastic Fluids: Enhanced Swimming at Large Helical Amplitudes, Phys. Rev. Lett. **111**, 068101 (2013).
[15] B. Thomases and R. D. Guy, Mechanisms of Elastic Enhancement and Hindrance for Finite-Length Undulatory Swimmers in Viscoelastic Fluids, Phys. Rev. Lett. **113**, 098102 (2014).
[16] B. Liu, T. R. Powers, and K. S. Breuer, Force-free swimming of a model helical flagellum in viscoelastic fluids, Proc. Natl. Acad. Sci. U.S.A. **108**, 19516 (2011).
[17] X. N. Shen and P. Arratia, Undulatory Swimming in Viscoelastic Fluids, Phys. Rev. Lett. **106**, 208101 (2011).
[18] E. Lauga, Propulsion in a viscoelastic fluid, Phys. Fluids **18**, 083104 (2007).
[19] J. Teran, L. Fauci, and M. Shelley, Viscoelastic Fluid Response Can Increase the Speed and Effciency of a Free Swimmer, Phys. Rev. Lett. **104**, 038101 (2010).
[20] J. P. Binagia, C. S. Guido, and E. S. G. Shaqfeh, Three-dimensional simulations of undulatory and amoeboid swimmers in viscoelastic fluids, Soft Matter **15**, 4836 (2019).
[21] A. Patteson, A. Gopinath, M. Goulian, and P. E. Arratia, Running and tumbling with E. coli in polymeric solutions, Sci. Rep. **5**, 15761 (2015).
[22] Jonathan P. Celli, Bradley S. Turner, Nezam H. Afdhal, Sarah Keates, Ionita Ghiran, Ciaran P. Kelly, Randy H. Ewoldt, Gareth H. McKinley, Peter So, Shyamsunder Erramilli, and Rama Bansil, Helicobacter pylori moves through mucus by reducing mucin viscoelasticity, Proc. Natl. Acad. Sci. U.S.A. **106**, 14321 (2009).
[23] Xingxiang Cao, Rama Bansil, K. Ramakrishnan Bhaskar, Bradley S. Turner, J. Thomas LaMont, Niu Niu, and Nezam H. Afdhal, ph-dependent conformational change of gastric mucin leads to sol-gel transition, Biophys. J. **76**, 1250 (1999).
[24] N. J. Balmforth, D. Coombs, and S. Pachmann, Microelasto hydrodynamics of swimming organisms near solid boundaries in complex fluids, Q. J. Mech. Appl. Math. **63**, 267 (2010).
[25] D. R. Hewitt and N. J. Balmforth, Taylor's swimming sheet in a yield-stress fluid, J. Fluid Mech. **828**, 33 (2017).
[26] D. R. Hewitt and N. J. Balmforth, Viscoplastic slender-body theory, J. Fluid Mech. **856**, 870 (2018).
[27] D. R. Hewitt and N. J. Balmforth, Locomotion with a wavy cylindrical filament in a yield-stress fluid, J. Fluid Mech. **936**, A17 (2022).
[28] Patrick S. Eastham, Hadi Mohammadigoushki, and Kourosh Shoele, Squirmer locomotion in a yield stress fluid, J. Fluid Mech. **948**, A54 (2022).
[29] Shijian Wu, Tomas Solano, Kourosh Shoele, and Hadi Mohammadigoushki, Formation of a strong negative wake behind a helical swimmer in a viscoelastic fluid, J. Fluid Mech. **942**, A10 (2022).

[30] See Supplemental Material at http://link.aps.org/supplemental/10.1103/PhysRevLett.130.114002 for additional details on the experimental setup, rheological properties of the fluids and the swimming data in yield stress as well as Newtonian fluids.

[31] Eric Lauga, *The Fluid Dynamics of Cell Motility*, Cambridge Texts in Applied Mathematics (Cambridge University Press, Cambridge, England, 2020).

[32] J. Gray and G. J. Hancock, The propulsion of sea-urchin spermatozoa, J. Exp. Biol. **32**, 802 (1955).

[33] Gaojin Li and Arezoo M. Ardekani, Undulatory swimming in non-Newtonian fluids, J. Fluid Mech. **784**, R4 (2015).

[34] S. Gomez, F. A. Godínez, E. Lauga, and R. Zenit, Helical propulsion in shear-thinning fluids, J. Fluid Mech. **812**, R3 (2017).

[35] M. Daneshi, A. Pourzahedi, D. M. Martinez, and D. Grecov, Characterising wall-slip behaviour of carbopol gels in a fully-developed poiseuille flow, J. Non-Newtonian Fluid Mech. **269**, 65 (2019).